



# Automated Driving for Global Nonpotential Simulations of the Solar Corona

Anthony R. Yeates<sup>1</sup> and Prantika Bhowmik<sup>1</sup>Department of Mathematical Sciences, Durham University, Durham, DH1 3LE, UK; [anthony.yeates@durham.ac.uk](mailto:anthony.yeates@durham.ac.uk)

Received 2022 March 18; revised 2022 June 24; accepted 2022 June 30; published 2022 August 9

## Abstract

We describe a new automated technique for active region emergence in coronal magnetic field models, based on the inversion of the electric field locally from a single line-of-sight magnetogram for each region. The technique preserves the arbitrary shapes of magnetic field distribution associated with individual active regions and incorporates emerging magnetic helicity (twist) in a parametrized manner through a noninductive electric field component. We test the technique with global magnetofrictional simulations of the coronal magnetic field during Solar Cycle 24 Maximum from 2011 June 1 to 2011 December 31. The active regions are determined in a fully automated and objective way using Spaceweather HMI Active Region Patch (SHARP) data. Our primary aim is to constrain two free parameters in the emergence algorithm: the duration of emergence and the twist parameter for each individual active region. While the duration has a limited effect on the resulting coronal magnetic field, changing the sign and amplitude of the twist parameters profoundly influences the amount of nonpotentiality generated in the global coronal magnetic field. We explore the possibility of constraining both the magnitude and sign of the twist parameter using estimates of the current helicity derived from vector magnetograms and supplied in the SHARP metadata for each region. Using the observed sign of twist for each region reduces the overall nonpotentiality in the corona, highlighting the importance of scatter in the emerging active region helicities.

*Unified Astronomy Thesaurus concepts:* [Solar magnetic fields \(1503\)](#); [Solar surface \(1527\)](#); [Solar atmosphere \(1477\)](#); [Active solar corona \(1988\)](#)

## 1. Introduction

In this paper we propose a technique for emerging active regions in data-driven simulations of the Sun's coronal magnetic field. The technique is designed for global-scale simulations of the coronal evolution over months to years, where multiple active regions are emerging and practical considerations prevent the detailed evolution within each individual active region from being followed. Our implementation is fully automated based on the Spaceweather HMI Active Region Patch (SHARP) data from the Helioseismic and Magnetic Imager (HMI) on Solar Dynamics Observatory (SDO; Bobra et al. 2014). However, the basic emergence technique could equally be applied to other data sources as it can also be used when only line-of-sight and not vector magnetograms are available.

Limiting the reliance on vector magnetograms is useful, partly so that the technique can be used to simulate periods when vector data are unavailable (either in the past or future), but also because of uncertainty in the horizontal/transverse magnetic field components in vector magnetograms (Metcalf et al. 2006; Wiegmann & Sakurai 2021). Particularly in the time-dependent simulations that we consider, errors in these components could lead to substantial spurious electric currents being generated in the corona (Metcalf et al. 2008; Wiegmann & Sakurai 2021). It should be emphasized that significant progress has been made in recent years in processing vector magnetograms to drive coronal simulations directly (for an example of the state-of-the-art, see Lumme et al. 2022). Nevertheless, such simulations require significant preprocessing at high resolution, and we opt for a simpler approach by

fitting only the line-of-sight magnetic field. In particular, this means that the quality of the resulting coronal magnetic field can be more easily controlled. This being said, we do explore how to utilize vector magnetic field data indirectly through the SHARP metadata, using the observed mean twist parameter to parameterize the magnetic helicity content of individual regions.

Our approach is to ingest magnetogram data only within active regions. Paradoxically, this is because active region emergence is only one driver of coronal magnetic evolution. Significant energy and magnetic helicity are also injected into the corona by surface motions on both small and large scales. In principle, full-disk observations of the magnetic field and/or plasma velocity in the solar photosphere could be used to drive simulations more or less directly (some efforts include Yang et al. 2012; Hayashi 2013; Weinzierl et al. 2016; Hayashi et al. 2021). However, the limitations of available observations restrict the accuracy of this approach at present. Not only are there no observations of the far side of the Sun, but the horizontal magnetic field components in vector magnetograms have significant uncertainties in weak magnetic field regions (Virtanen et al. 2019). Even static extrapolations from vector magnetograms in these regions are unable to recover large-scale coronal current structures such as filament channels. Yet these are observed indirectly to have significantly nonpotential magnetic fields (Mackay et al. 2010). Therefore, our approach is to use magnetogram observations only within active regions, with evolution over the rest of the solar surface envisaged to be simulated by imposing flows on either large or small scales.

The new emergence technique improves on previous global simulations by our group and collaborators because it allows the active regions to have more realistic shapes, matching the observed patterns of radial magnetic field on the photosphere. Previous simulations used idealized, symmetric magnetic bipoles with a fixed functional form (Mackay & van



Original content from this work may be used under the terms of the [Creative Commons Attribution 4.0 licence](#). Any further distribution of this work must maintain attribution to the author(s) and the title of the work, journal citation and DOI.

Ballegooijen 2001), with only overall properties such as magnetic flux, size, and tilt angle constrained to observations (Yeates et al. 2008). This had the advantage that the regions could easily be inserted in three dimensions, and given an arbitrary amount of magnetic helicity (e.g., Mackay & van Ballegooijen 2005; Yeates et al. 2008). However, there were limitations to this approach. For example, the fitting of bipoles to complex active regions had to be done manually, so it was not fully objective. And recent work with surface flux transport models has found that the assumption of symmetric and bipolar shapes can lead to inaccurate estimates of the net end-of-cycle polar field remaining from the decay of many active regions over the 11 yr solar cycle (Iijima et al. 2019; Jiang et al. 2019; Yeates 2020a). Thus for simulations over periods of years, allowing arbitrary shapes is a desirable improvement.

In order to allow for arbitrary active region shapes, we emerge the regions not by suddenly inserting three-dimensional magnetic fields as before, but rather by imposing an electric field on the solar surface over a finite time interval. For coronal simulations, it is consistent to impose only the horizontal electric field components (e.g., Cheung & DeRosa 2012). The approach of emerging flux by imposing an electric field was used by Fan & Gibson (2004) to emerge a twisted magnetic flux tube into a pre-existing coronal arcade. Those authors imposed a time-dependent electric field so as to control the three-dimensional magnetic field structure that was emerging. Here, we instead impose a steady electric field to build a final radial magnetic field distribution in the photosphere that matches observations. Since we determine this electric field from the magnetic field by inverting Faraday’s Law, it is not unique (Fisher et al. 2020), but is determined only up to an unknown gradient term, known as the “noninductive” electric field (Fisher et al. 2010). Studies comparing reconstructed electric fields to ground truth from magnetohydrodynamic (MHD) simulations find that the noninductive contribution is typically significant in active regions (Fisher et al. 2012; Kazachenko et al. 2014). Indeed, Pomoell et al. (2019) found that a significant noninductive contribution was required to reproduce an observed flux rope eruption in a data-driven simulation. And even systematic flows such as differential rotation can lead to a significant noninductive component (Weinzierl et al. 2016). Since we do not follow the detailed evolution during the emergence process itself, we do not attempt to infer the noninductive electric field directly from observations (see Fisher et al. 2020), but rather incorporate it in an ad-hoc parametrized way (Cheung & DeRosa 2012; Lumme et al. 2017; Yardley et al. 2018). This allows us to control the amount of magnetic helicity in each emerging region. The most conservative approach, with minimal nonpotential energy injection, would be to neglect the noninductive contribution altogether (e.g., Mackay et al. 2011; Yang et al. 2012; Hayashi et al. 2018; Yardley et al. 2021). We will illustrate the effect of this emerging helicity on the resulting global coronal field.

This paper is organized as follows. Section 2 describes our emergence technique using the “local inductive” electric field, along with the additional noninductive contribution that injects magnetic helicity in the emerging region. To test the global impact of key parameters in the new technique, we use magnetofrictional simulations, as described in Section 3. An important parameter controls the amount of helicity injection in each region, and the choice of this parameter is discussed in

Section 4. Results of the tests with different parameters are given in Section 5 and the conclusions are in Section 6.

## 2. Emergence Algorithm

The purpose of our emergence algorithm is to take a single radial-component magnetogram for an active region,  $B_r(\theta, \phi)$ , and determine a suitable horizontal electric field  $\mathbf{E}_\perp(\theta, \phi, t)$  that can be applied to emerge the region in a three-dimensional coronal simulation. In our implementation, we assume that this magnetogram  $B_r(\theta, \phi)$  is (i) defined on a uniform grid in  $s \equiv \cos \theta$  (sine latitude) and  $\phi$  (longitude) and (ii) flux balanced in the sense that  $\int_S B_r(\theta, \phi) \sin \theta \, d\theta \, d\phi = 0$ , where  $S$  is the solar surface, and (iii) has localized support, in the sense that  $B_r = 0$  outside some region  $D \subset S$ . Thus we also have local flux balance,  $\int_D B_r(\theta, \phi) \sin \theta \, d\theta \, d\phi = 0$ . In our simulations described in Sections 3 and 5, this  $B_r(\theta, \phi)$  with compact support will emerge on top of a pre-existing magnetic field distribution that fills the whole solar surface. Moreover, the local emergence electric field will be superimposed on the global electric field that describes ongoing large-scale and small-scale surface flows.

### 2.1. Test Data

To illustrate the electric field computation we will use an active region from the automatically generated HMI/SHARP database (Bobra et al. 2014), shown in Figure 1. A single line-of-sight magnetogram was selected when the region was close to Central Meridian. Following the methodology of Yeates (2020a), this has been (i) downsampled to the  $180 \times 360$  grid in  $(s, \phi)$  used throughout this paper, and (ii) corrected for flux balance. As discussed in the introduction, we use only line-of-sight magnetograms and hence choose a magnetogram near Central Meridian so as to reduce projection effects. This does have the consequence that any flux emergence after the region has passed Central Meridian will be missed, but this is a limitation of the input data rather than the emergence algorithm described in this section.

### 2.2. Time Dependence

Since our data comprise a single magnetogram for each active region, we assume that every region emerges over a fixed time interval  $T_{\text{em}}$ , typically chosen as 24 hr, although the effect of this parameter will be considered in Section 5.1. During this interval we impose a steady electric field  $\mathbf{E}_\perp(s, \phi)$  satisfying

$$-\hat{r} \cdot \nabla \times \mathbf{E}_\perp(s, \phi) = \frac{B_r(s, \phi)}{T_{\text{em}}}, \quad (1)$$

so that the required  $B_r(s, \phi)$  distribution is superimposed at the end of this emergence on any pre-existing  $B_r$  distribution (which is usually weak in our simulations). The assumption of a steady emergence rate is reasonable for global simulations that focus on the postemergence evolution over longer timescales. In fact, piecewise-steady electric fields were also used to interpolate between subsequent magnetograms in the active region simulations of Mackay et al. (2011) and Cheung & DeRosa (2012).

Although any  $\mathbf{E}_\perp$  satisfying (1) will generate the same  $B_r$  on the surface, different choices could lead to different coronal magnetic fields when used as boundary conditions for three-

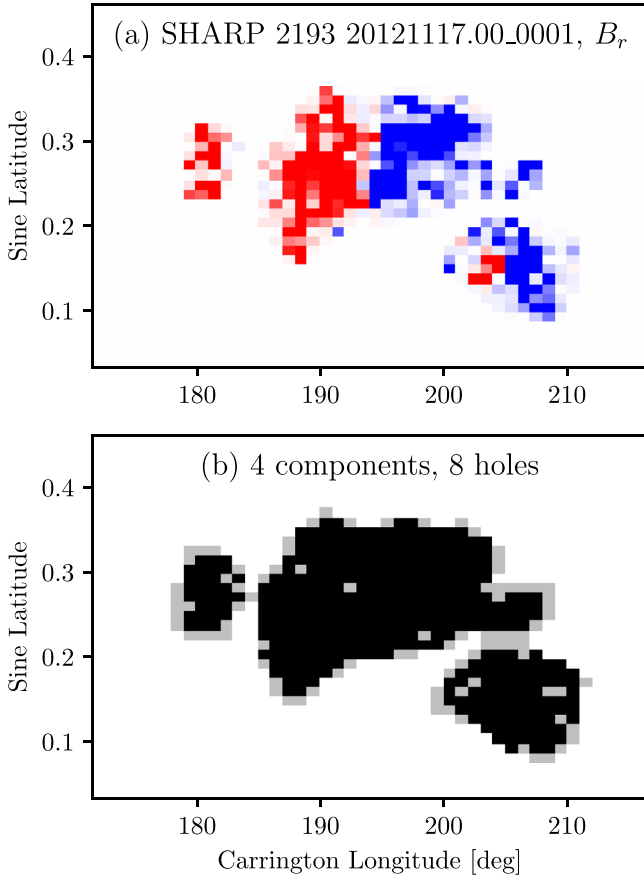


**Figure 1.** Magnetogram for an example SHARP (a) and the corresponding emergence region (b). Black pixels show the region  $D$  before smoothing, which had four separate components and eight holes. Gray pixels show the simply connected region  $\bar{D}$  resulting from smoothing, having only a single component and no holes. In (a), red denotes positive  $B_r$  and blue negative, saturated at  $\pm 50$  G.

dimensional simulations. Our approach is to decompose  $\mathbf{E}_\perp$  into two contributions:

$$\mathbf{E}_\perp(s, \phi) = \mathbf{E}_\perp^0(s, \phi) - \nabla \frac{\Psi(s, \phi)}{T_{\text{em}}}. \quad (2)$$

The first term  $\mathbf{E}_\perp^0$  is the inductive component of the emergence electric field, and as such will generate a coronal magnetic field of minimum possible complexity. Our method for computing this term is described in Section 2.3. The other term is the noninductive component that does not change the corresponding magnetogram  $B_r$  but allows us to vary the free energy of the emerging regions. This twisting potential  $\Psi$  is discussed in Section 2.4.

### 2.3. Local Inductive Electric Field

From the original local region  $D$ —which may consist of several disconnected pieces—we first identify a simply connected region,  $\bar{D}$ , containing the newly emerging flux. Our aim is to compute an electric field that vanishes outside this region. As an illustration, consider the region shown in Figure 1. The black shading in Figure 1(b) shows the original region,  $D$  (chosen as  $|B_r| > 10^{-3}$  G). This is not simply connected, having several disconnected components containing holes. However, our algorithm for calculating  $\mathbf{E}_\perp^0$  requires a single simply connected region. From  $D$ , we apply successive

steps of Gaussian smoothing to  $|B_r|$  until such a region  $\bar{D}$  is reached, shown by the wider gray area in Figure 1(b).

The electric field is computed only on  $\bar{D}$ , with the boundary condition  $\mathbf{E}_\perp \times \mathbf{n} = 0$  on the boundary  $\partial\bar{D}$ , consistent with magnetic flux balance in  $\bar{D}$ . A staggered grid is used where  $B_r^{i,j}$  is defined at the cell centers,  $E_s^{i,j+1/2}$  is defined on the  $s$ -edges and  $E_\phi^{i+1/2,j}$  is defined on the  $\phi$ -edges (e.g., Figure 2). Here  $i$  and  $j$  denote the latitudinal ( $s$ ) and azimuthal ( $\phi$ ) indices of the cell. Thus with Stokes’ Theorem applied to Equation (1),  $E_s^{i,j+1/2}$  and  $E_\phi^{i+1/2,j}$  must satisfy

$$\begin{aligned} (\ell_s E_s)^{i,j-1/2} - (\ell_s E_s)^{i,j+1/2} + (\ell_\phi E_\phi)^{i+1/2,j} \\ - (\ell_\phi E_\phi)^{i-1/2,j} = \frac{R_\odot^2 \Delta s \Delta \phi B_r^{i,j}}{T_{\text{em}}}, \end{aligned} \quad (3)$$

where  $R_\odot^2 \Delta s \Delta \phi$  is the area of a grid cell—uniform in these coordinates. The cell edge lengths are given by  $\ell_s^{i,j+1/2} = R_\odot [\arcsin(s^{i+1/2}) - \arcsin(s^{i-1/2})]$  and  $\ell_\phi^{i+1/2,j} = R_\odot \Delta \phi \sqrt{1 - (s^{i+1/2})^2}$ . The boundary condition is enforced by setting tangential components of  $E_s^{i,j+1/2}$  or  $E_\phi^{i+1/2,j}$  to zero on the boundary edges of  $\bar{D}$ , shown by dashed lines in Figure 2.

When applied to each grid cell in  $\bar{D}$ , Equation (3) gives a system of linear equations for  $E_s^{i,j+1/2}$  and  $E_\phi^{i+1/2,j}$ . The system is underdetermined, reflecting the freedom to add an arbitrary gradient term to  $\mathbf{E}_\perp$  without affecting  $\hat{\mathbf{r}} \cdot \nabla \times \mathbf{E}_\perp$ . Our implementation solves for  $(\ell_s E_s)^{i,j+1/2}$  and  $(\ell_\phi E_\phi)^{i+1/2,j}$ , since these weighted values are most useful in the magnetofrictional code used for our tests (Section 5). We choose the least-squares solution,  $\mathbf{E}_\perp^0$ , to this system, i.e., the solution that minimizes the  $L_2$ -norm. This is implemented with a sparse matrix and a sparse least-squares solver (in Python). This is mathematically equivalent to finding an electric field of the form  $\mathbf{E}_\perp^0 = -\nabla \times (\Phi \hat{\mathbf{r}})$ , which is an inductive electric field (Yeates 2017). However, unlike the inductive electric fields computed by Weinzierl et al. (2016) or Yeates (2017), who solved Equation (3) over the full solar surface, here we have allowed nonzero electric field only within the region  $\bar{D}$ . Hence, we call this a “local inductive” electric field solution. The resulting  $E_s^0$  and  $E_\phi^0$  are shown in Figures 3(a) and (e).

Although this solution  $\mathbf{E}_\perp^0$  satisfies  $\mathbf{E}_\perp \times \mathbf{n} = 0$  on  $\partial\bar{D}$ , Figures 3(a) and (e) show that the normal component  $\mathbf{E}_\perp^0 \cdot \mathbf{n}$  can be discontinuous at the edge of  $\bar{D}$ . While this does not affect  $\hat{\mathbf{r}} \cdot \nabla \times \mathbf{E}_\perp$ , it could lead to the generation of spurious currents in coronal simulations. We remove the sharp discontinuity by smoothing  $\mathbf{E}_\perp^0$  with an evolution of the form

$$\frac{\partial \mathbf{E}_\perp^0}{\partial t} = \nabla (\nabla \cdot \mathbf{E}_\perp^0). \quad (4)$$

This leaves  $\hat{\mathbf{r}} \cdot \nabla \times \mathbf{E}_\perp^0$  unaffected provided the gradient is discretized consistently, which we ensure by using the staggered form

$$\begin{aligned} (\ell_s E_s)_{k+1}^{i,j+1/2} &= (\ell_s E_s)_k^{i,j+1/2} \\ &+ \Delta t (D_k^{i+1/2,j+1/2} - D_k^{i-1/2,j+1/2}), \end{aligned} \quad (5)$$

$$\begin{aligned} (\ell_\phi E_\phi)_{k+1}^{i+1/2,j} &= (\ell_\phi E_\phi)_k^{i+1/2,j} \\ &+ \Delta t (D_k^{i+1/2,j+1/2} - D_k^{i+1/2,j-1/2}), \end{aligned} \quad (6)$$

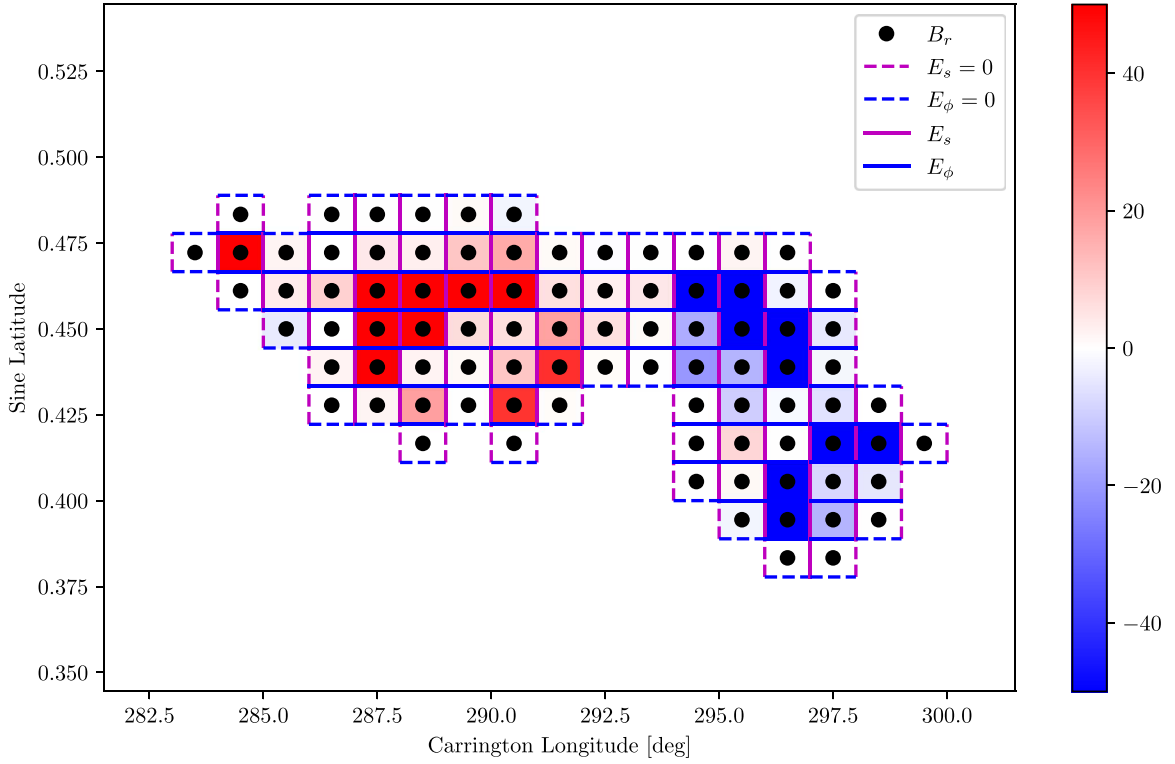


**Figure 2.** Example of the local staggered grid for a newly emerging region (where for clarity we choose a smaller region than Figures 1 and 3). Red/blue background shading shows  $B_r$  (saturated at  $\pm 50$  G), located at the cell centers (black dots). Unknown values of  $E_s$  and  $E_\phi$  are located on the vertical and horizontal edges, respectively magenta and blue. Boundary edges where  $E_s = 0$  or  $E_\phi = 0$  are shown dashed.

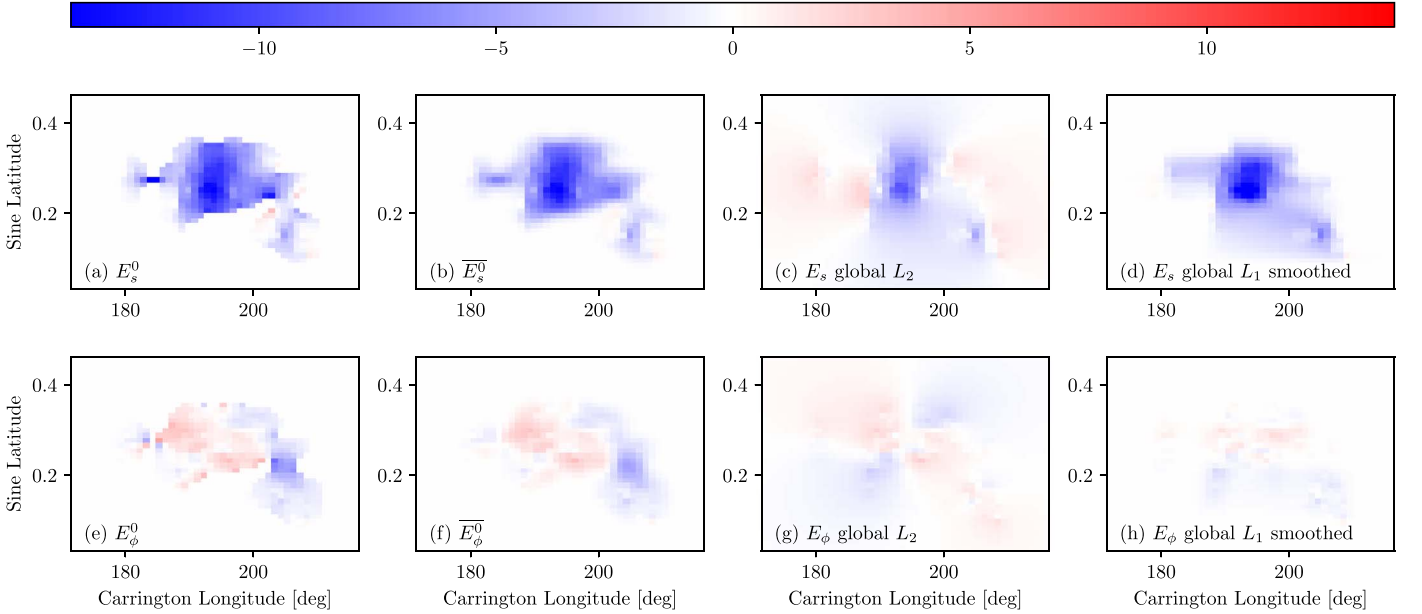


**Figure 3.** Computed electric field  $\mathbf{E}_\perp$  for the region shown in Figure 1. Columns show  $E_s$  and  $E_\phi$  components for different solutions: the local inductive solution before (a/e) and after (b/f) smoothing, the global inductive solution (c/g), and the global sparse solution (d/h). Units are  $\text{V m}^{-1}$ , and all plots are saturated at the same maximum value. All four electric fields generate the same  $B_r$  distribution.

where  $D_k^{i+1/2, j+1/2}$  is a finite-difference approximation to  $\nabla \cdot \mathbf{E}_\perp^0$  at time step  $k$ . The step size  $\Delta t$  is chosen for numerical stability and we integrate for a total time  $\approx 7 \times 10^{-5} T$ , where  $T$  is the time that would be taken to diffuse a distance  $R_\odot$ . We choose this short integration time to minimize the amount of smoothing, which is a balance between reducing currents at the edge of  $\bar{D}$  and maintaining localization of  $\mathbf{E}_\perp^0$ . If the amount of

smoothing were increased,  $\mathbf{E}_\perp^0$  would eventually tend toward the global inductive solution. The result with our chosen amount of smoothing is illustrated in Figures 3(b) and (f). We denote this smoothed local inductive electric field by  $\overline{\mathbf{E}_\perp^0}$ , and use it in practice for the  $\mathbf{E}_\perp^0$  component in Equation (2).

It is worth noting that  $\overline{\mathbf{E}_\perp^0}$  differs significantly from electric fields that have previously been used to drive magnetofrictional

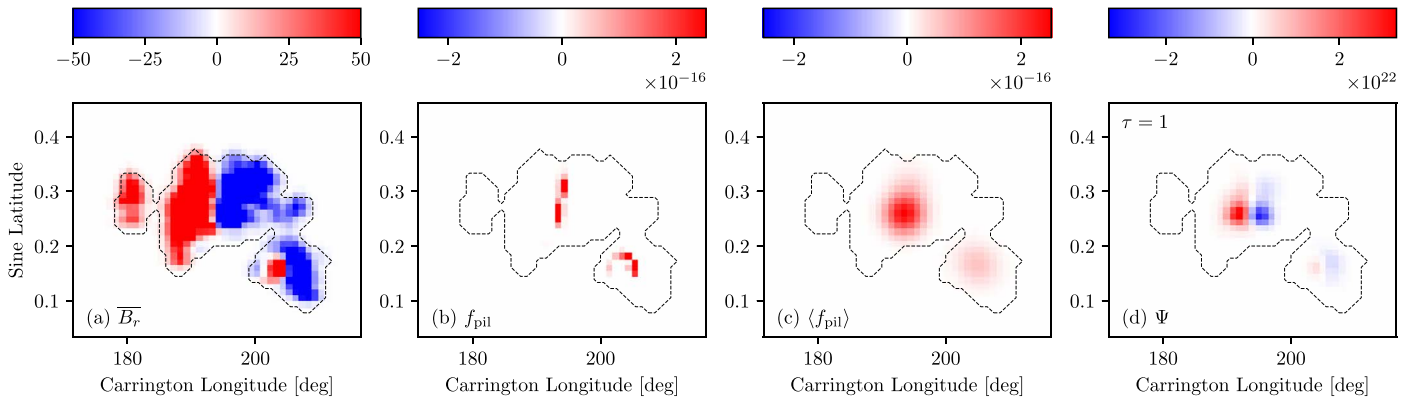


**Figure 4.** Construction of the twisting potential  $\Psi(s, \phi)$  for an example region (the same shown in Figures 1 and 3), with  $\tau = 1$ . Units are G for  $\overline{B}_r$ ,  $\text{G}^2 \text{cm}^{-2}$  for  $f_{\text{pil}}$ , and  $\text{G cm}^2$  for  $\Psi$ .

simulations. For example, Figures 3(c) and (g) show the components of the global inductive solution, which satisfies  $\mathbf{E}_\perp = -\nabla \times (\Phi \hat{\mathbf{r}})$  on the whole spherical surface. By definition, this minimizes the  $L_2$ -norm of  $\mathbf{E}_\perp$  ( $70 \text{ V m}^{-1}$  compared to  $111 \text{ V m}^{-1}$  for the local inductive solution), but at the expense of spreading nonzero  $\mathbf{E}_\perp$  far outside of  $\overline{D}$ , decaying only as the inverse of the distance from  $\overline{D}$  (Yeates 2017). Although no additional  $B_r(R_\odot, s, \phi)$  is generated by this nonzero  $\mathbf{E}_\perp$  outside  $\overline{D}$ , additional electric fields are generated and these can change the evolution of the coronal magnetic field outside of the emergence region (illustrated in Section 5.3 below). Thus our local inductive  $\overline{\mathbf{E}}_\perp^0$  is more appropriate for incorporating newly emerging regions in global simulations.

As a further comparison, Figures 3(d) and (h) show a sparse  $\mathbf{E}_\perp$  computed over the whole solar surface for this region, using the  $L_1$ -minimization method of Yeates (2017). Because it is essentially a compromise between sparsity (localization) and smoothness, the  $\mathbf{E}_\perp$  generated by the sparse algorithm is less smooth than our  $L_2$ -based electric fields. For a fairer comparison, the solution shown in Figures 3(d) and (h) has had the same smoothing applied via Equation (4). It is clear that the global sparse  $\mathbf{E}_\perp$  shares some of the broad features of the local inductive solution, with  $|E_s| > |E_\phi|$  overall and localization around  $\overline{D}$ . However, there are two disadvantages of the sparse solution. First, although it is localized, it is not necessarily localized specifically to the region  $\overline{D}$ , as in this example. Second, the sparse solution is more expensive to compute because it requires multiple least-squares solutions over the whole solar surface, in an iterative loop, rather than a single solution over only the local region  $\overline{D}$ . Thus we find that the local inductive  $\overline{\mathbf{E}}_\perp^0$  is an improvement. Note that, although it does not concern us here, the sparse solution is also found to lead to significant spurious coronal currents when applied with higher-cadence sequences of observational magnetograms (Mackay & Yeates 2021). Since minimizing the  $L_1$  norm is equivalent to finding the sparsest solution, we can compare the relative sparseness of the different  $\mathbf{E}_\perp$  by their  $L_1$  norms, which for this example are  $2256 \text{ V m}^{-1}$  for the local inductive solution,  $6115 \text{ V m}^{-1}$  for the global inductive solution, and  $1978 \text{ V m}^{-1}$  for the global sparse solution. Thus—as is seen in Figure 3—the local inductive solution does not have a significantly larger footprint than the sparse solution itself, even after the smoothing step.

#### 2.4. Helicity Injection

The noninductive electric field, resulting from  $-\nabla(\Psi/T_{\text{em}})$  in Equation (2), typically increases both the Poynting flux of magnetic energy and the flux of magnetic helicity into the corona (Kazachenko et al. 2014; Pomoell et al. 2019). Indeed, the existence of nonzero free magnetic energy is an important feature of many real active regions. While we do not follow the detailed injection of this free energy during the emergence process, it is nevertheless important to account for the net emergence of any nonpotential structure. Thus we include a nonzero “twisting” component  $-\nabla(\Psi/T_{\text{em}})$ . In line with observations and the theory of helicity condensation, we choose to concentrate this twisting near polarity inversion lines, similar to Mikić et al. (2018; see also Mackay et al. 2018; Yeates et al. 2018). The choice of twisting potential  $\Psi(s, \phi)$  will not affect  $\hat{\mathbf{r}} \cdot \nabla \times \mathbf{E}_\perp$ , but it will lead to the generation of additional  $B_s$  and  $B_\phi$  components in the corona since it is imposed only at  $r = R_\odot$ . Note that Mackay et al. (2018) instead modified  $\mathbf{E}$  by adding an  $E_r$  component (in their case, through modifying  $\mathbf{A}$ ), but the effect on  $\mathbf{B}$  is the same, the difference being only in choice of noninductive component.

The potential  $\Psi(s, \phi)$  for a given region is constructed as follows, illustrated in Figure 4:

1. Polarity inversion lines are identified using the function

$$f_{\text{pil}}(s, \phi) = (|\nabla \overline{B}_r| - |\nabla |\overline{B}_r||)^2, \quad (7)$$

where  $\overline{B}_r$  is a smoothed  $B_r$  distribution, computed by mild Gaussian smoothing with a standard deviation of less than one grid cell (Figure 4(a)). The function  $f_{\text{pil}}$  is nonzero near polarity inversion lines and zero away from them. It is strongest where the gradient of  $B_r$  is strongest (Figure 4(b)).

2. A somewhat broader twisting region is defined by Gaussian smoothing of  $f_{\text{pil}}$  with a standard deviation of two grid cells to give  $\langle f_{\text{pil}} \rangle$ . This is chosen approximately so as to localize the twisting within the interior of  $\overline{D}$  (Figure 4(c)).
3. The potential is then

$$\Psi(s, \phi) = \tau b_0 \langle f_{\text{pil}} \rangle \overline{B}_r, \quad (8)$$

as shown in Figure 4(d). Here  $b_0$  is a constant normalization factor, chosen so that

$\max|\nabla\Psi| = \tau L \max|\overline{B}_r|$ . The dimensionless “twist” parameter  $\tau$  is signed such that  $\tau > 0$  leads to positive helicity (sinistral chirality) and  $\tau < 0$  to negative helicity (dextral chirality). We set  $L = 0.015R_\odot$ , which is the height of the first coronal grid cell in our magnetofrictional calculations. With this normalization, the horizontal field strength generated by the twisting should be roughly of the order  $|\tau B_r|$ .

### 3. Magnetofrictional Simulations

To test our emergence algorithm, we use a global magnetofrictional model. The electric fields from our emergence algorithm could equally be applied to any other evolving MHD model of the coronal magnetic field, but at present the magnetofrictional approach is the most practical for simulating the large-scale coronal evolution over long timescales. This allows us to determine the likely wider consequences of choosing different parameters  $T_{\text{em}}$  and  $\tau$  in our emergence model.

#### 3.1. Global Magnetofrictional Model

The coupled surface flux transport and magnetofrictional approach were first introduced by van Ballegoijen et al. (2000), and later Yeates et al. (2008) extended it to cover the global corona. The basic idea is that the coronal magnetic field  $\mathbf{B}$  evolves continuously through a sequence of nonpotential states in response to the changing surface boundary. Large-scale plasma motions and magnetic diffusion on the surface drive the coronal field evolution in a quasi-static manner. In the corona, we solve for the magnetic vector potential  $\mathbf{B} = \nabla \times \mathbf{A}$ ,

$$\frac{\partial \mathbf{A}}{\partial t} = -\mathbf{E}, \quad (9)$$

where  $\mathbf{E} = -\mathbf{v} \times \mathbf{B} + \mathbf{N}$ . Here,  $\mathbf{E}$  and  $\mathbf{N}$  represent the electric field, and the nonideal part of Ohm’s law, respectively. Although the corona is highly conducting, the nonideal term reflects the fact that we are modeling the large-scale, mean magnetic field; thus  $\mathbf{N}$  describes the effect of unresolved smaller-scale turbulent motions (van Ballegoijen et al. 2000). The velocity  $\mathbf{v}$  in the corona—discussed in the next paragraph—is a combination of frictional relaxation and a solar wind outflow. On the lower boundary, we apply a different electric field which is a superposition of (i) the emergence electric fields  $\mathbf{E}_\perp$  for individual active regions, as per Section 2, and (ii) a global electric field  $\mathbf{E}_\perp = -\mathbf{v}_s \times (B_r \hat{\mathbf{r}}) + \eta_0 \nabla \times (B_r \hat{\mathbf{r}})$ . Here the large-scale velocity  $\mathbf{v}_s(\theta)$  on the lower surface mimics two large-scale plasma flows: meridional circulation and differential rotation (for more details, see Section 2.2 of Yeates 2014). The surface diffusivity  $\eta_0 = 455 \text{ km}^2 \text{ s}^{-1}$  represents the net effect of small-scale (supergranular) flows. The computational domain extends radially within  $R_\odot \leq r \leq 2.5 R_\odot$  and includes the full extent of colatitude  $0^\circ$ – $180^\circ$  and longitude  $0^\circ$ – $360^\circ$ . We solve Equation (9) using a finite-difference method on an equally spaced grid of  $60 \times 180 \times 360$  cells in  $\log(r/R_\odot)$ , sine latitude, and longitude.

This nonpotential coronal model is a simplified version of full-scale MHD models. We do not solve the full momentum equation to simulate the velocity evolution, but rather employ a “frictional” velocity  $\mathbf{v}$  proportional to the Lorentz force. Such

an artificial velocity field drives the coronal magnetic field toward a force-free equilibrium,  $\mathbf{J} \times \mathbf{B} = 0$  where  $\mathbf{J} = \nabla \times \mathbf{B}$ . The velocity field within the corona is modeled accordingly as

$$\mathbf{v} = \frac{\mathbf{J} \times \mathbf{B}}{\nu} + v_{\text{out}}(r) \hat{\mathbf{r}} \quad (10)$$

where  $\nu = \nu_0 |\mathbf{B}|^2 / (r^2 \sin^2 \theta)$ , is the friction coefficient, with  $\nu_0 = 2.8 \times 10^5 \text{ s}$ . On the photosphere, the frictional velocity is set to zero. The second term in Equation (10), with  $v_{\text{out}}(r) = v_0 (r/R_\odot)^{11.5}$  and  $v_0 = 100 \text{ km s}^{-1}$ , models (crudely) the effect of the solar wind in the upper corona (see Rice & Yeates 2021). It ensures that magnetic field lines become essentially radial by  $2.5 R_\odot$ , except temporarily during eruptions. All components of  $\mathbf{B}$  are periodic in  $\phi$ . At the inner ( $1.0 R_\odot$ ) and outer ( $2.5 R_\odot$ ) boundaries the transverse current density,  $\mathbf{J} \times \hat{\mathbf{r}}$ , is set to zero, such that the Lorentz force is always tangential to the boundaries. The nonideal term  $\mathbf{N}$  is modeled using fourth-order hyperdiffusion, which preserves magnetic helicity density  $\mathbf{A} \cdot \mathbf{B}$  in the volume (van Ballegoijen & Cranmer 2008). We use,  $\mathbf{N} = -(\mathbf{B}/|\mathbf{B}|^2) \nabla \cdot (\eta_h |\mathbf{B}|^2 \nabla \alpha)$ , where  $\alpha = \mathbf{J} \cdot \mathbf{B} / |\mathbf{B}|^2$  and  $\eta_h = 10^{31} \text{ cm}^4 \text{ s}^{-1}$ .

#### 3.2. Simulation Duration and Input Data

We perform three-dimensional magnetofriction simulations for 213 days, covering 2011 June 1 to 31 2011 December 31, around the Solar Cycle 24 Maximum. A three-dimensional magnetic field distribution is required to initialize the simulation, which we obtain from a potential field source surface extrapolation (Yeates 2018) from the HMI radial-component pole-filled Carrington map 2210 (Sun 2018).

The emerging regions during this period are extracted automatically from the HMI/SHARP database, using the methodology of Yeates (2020a), which is fully automated and repeatable (the code is freely available at Yeates 2022). In summary, a single line-of-sight magnetogram is selected at the time when the region was closest to Central Meridian. The extraction code discards those SHARPs that are either too small to resolve at the chosen  $180 \times 360$  resolution, have highly imbalanced flux (near unipolar), or represent a repeat observation of an earlier region surviving on the solar surface for more than one Carrington rotation. This leaves 102 active regions with realistic shapes to emerge in the magnetofrictional simulations, using our new emergence technique described in Section 2.

#### 3.3. Diagnostic Tools

Since our simulations model solar maximum with a hundred active regions emerging, the coronal magnetic field evolution is quite dynamic, with numerous nonpotential structures forming and erupting. Thus, unlike the solar minimum study by Bhowmik & Yeates (2021), where individual nonpotential structures were tracked and analyzed over a few days, here we primarily focus on global measures of nonpotentiality in the three-dimensional coronal magnetic field. The temporal evolution of these measures is depicted in Figure 5 for a particular magnetofrictional simulation where active regions have emergence duration  $T_{\text{em}} = 24 \text{ hr}$  and all have the same twist  $\tau = \pm 0.1$  (positive in the southern hemisphere, negative in the northern hemisphere).

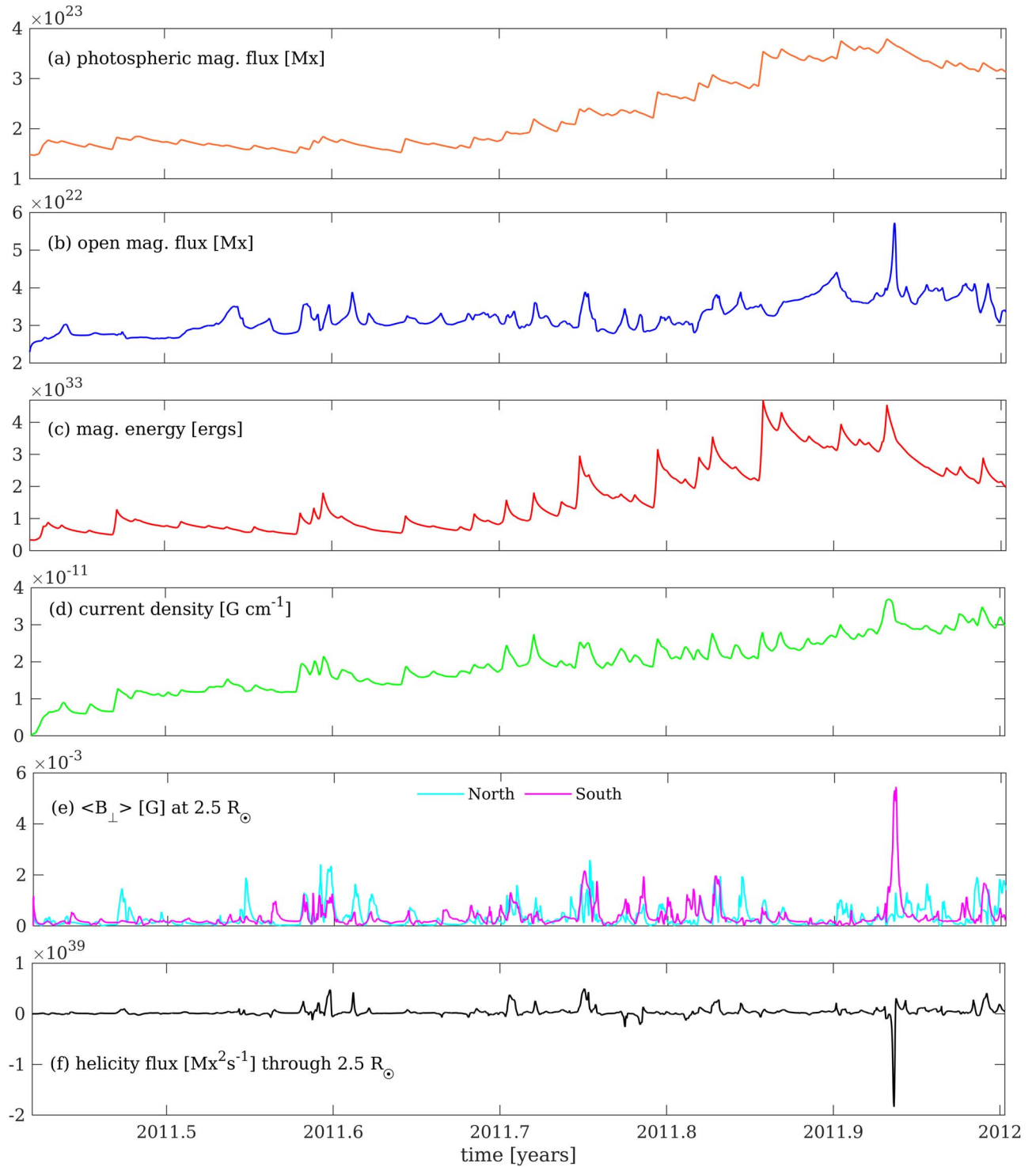


**Figure 5.** Temporal evolution of global quantities, in the run with  $T_{\text{em}} = 24$  hr and  $\tau = 0.1$  (with sign given by the majority hemispheric rule). From top to bottom: (a) unsigned photospheric magnetic flux, (b) unsigned open magnetic flux, (c) total magnetic energy, (d) mean current density, (e) horizontal components of the magnetic field at the outer boundary in separate hemispheres, and (f) helicity flux through the outer boundary.

Figure 5(a) shows the evolution of the photospheric magnetic flux calculated by integrating  $|B_r|$  over the surface  $r = R_\odot$ . The sudden rises in photospheric flux denote the epochs of active region emergence. Besides the newly emerged active regions, any significant changes in the coronal magnetic field distribution, especially at the outer boundary ( $2.5 R_\odot$ ), are caused by eruptions of coronal structures. These need not be directly caused by active region emergence, as seen in

Figure 5(b), which shows the open magnetic flux (integral of  $|B_r|$  over the surface  $r = 2.5 R_\odot$ ). Figure 5(c) shows the total magnetic energy in the corona, calculated by integrating  $|\mathbf{B}|^2 / (8\pi)$  over the whole simulation volume. Another important measure is the mean current density  $|\mathbf{J}|$  per unit volume within the corona, shown in Figure 5(d). The current density is directly linked with the nonpotential part of the magnetic field.

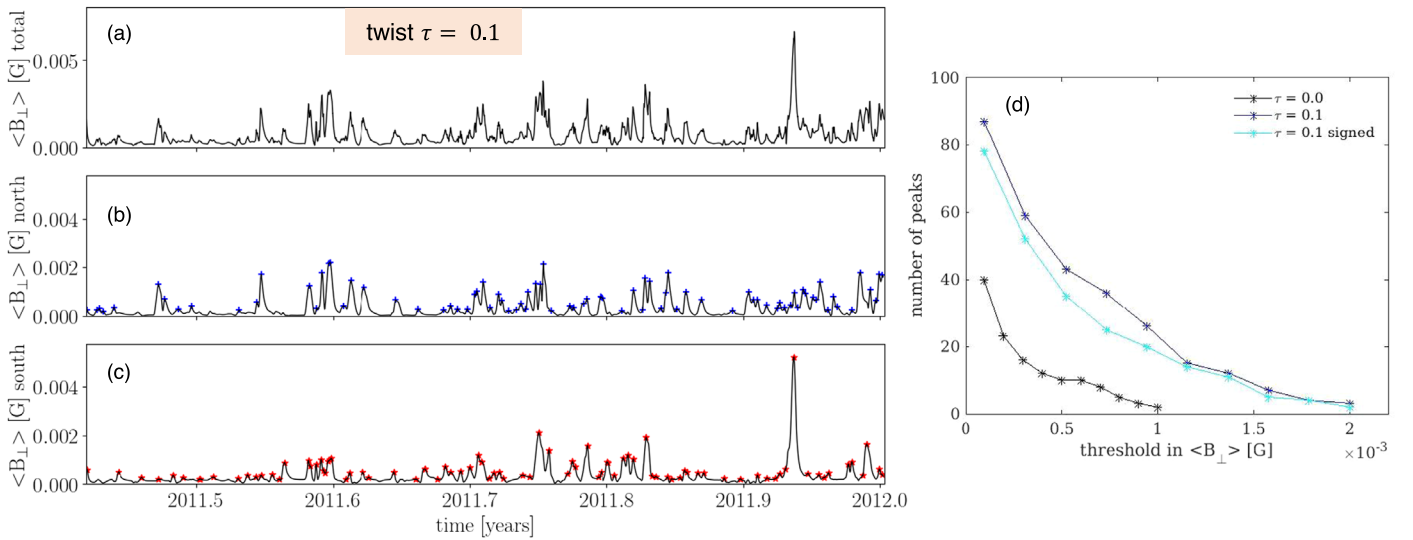


**Figure 6.** Selection of peaks in  $B_{\perp}$ , for the simulation shown in Figure 5. Panels (a–c) show averages  $\langle B_{\perp} \rangle$  over respectively the full outer boundary, the northern hemisphere only, and the southern hemisphere only. Identified peaks with the threshold  $3 \times 10^{-4}$  G are shown by blue and red asterisks. Panel (d) shows how the number of identified peaks varies with this threshold.

We also study the evolution of the average horizontal magnetic field,  $B_{\perp} = (B_{\theta}^2 + B_{\phi}^2)^{1/2}$ , at  $r = 2.5 R_{\odot}$ . The coronal magnetic field at the outer boundary is primarily radial due to the solar wind. However,  $B_{\perp}$  becomes significantly enhanced when any nonpotential coronal magnetic structure erupts and passes through the outer boundary (Yeates & Hornig 2016; Lowder & Yeates 2017; Bhowmik & Yeates 2021). The temporal evolution of the average  $\langle B_{\perp} \rangle$  over the surface  $r = 2.5 R_{\odot}$  is depicted in Figure 5(e), where we separate the averages in the northern and southern hemispheres.

The bottom row, Figure 5(f), shows the evolution of (relative) helicity flux through the outer boundary. Helicity is injected into the coronal magnetic field through large-scale shearing by differential rotation as well as the emergence of twisted active regions. With hyperdiffusion, the volume dissipation of helicity is negligible, with only an extremely small amount from numerical diffusion (e.g., Figure 1 of Bhowmik & Yeates 2021). Thus the ejection of unstable nonpotential structures with high helicity content through the outer boundary is the prime means by which the coronal model sheds helicity. The total (signed) flux of relative helicity through the outer boundary is gauge independent and computed by integrating  $\tilde{\mathbf{A}} \times (2\mathbf{E} + \partial\tilde{\mathbf{A}}/\partial t)$  over the surface  $r = 2.5 R_{\odot}$ , where  $\tilde{\mathbf{A}}$  is an appropriately chosen vector potential that must be computed from  $\mathbf{B}$  (for details, see Yeates & Hornig 2016).

As discussed already,  $B_{\perp}$  is a useful indicator for eruptions of nonpotential coronal structures, as well as the amount of magnetic flux involved. We calculate  $\langle B_{\perp} \rangle$  at  $2.5 R_{\odot}$  at a cadence of 20 s; thus, individual peaks with significant amplitudes can be considered to be associated with separate eruptions. As an indicator of the number of eruptions, we count the number of peaks in  $\langle B_{\perp} \rangle$  (for each hemisphere separately). The total number of peaks will depend on the particular threshold of  $B_{\perp}$  imposed for selecting the peaks. Figures 6(a)–(c) show the selected peaks with asterisks for a reasonable choice of the threshold. Figure 6(d) depicts how the number of peaks (in the northern hemisphere) varies with an increasing threshold value, and for simulations with different active region twists  $\tau$  (to be discussed in the following section). The

simulation that is shown in Figures 5 and 6(a)–(c) is the dark blue curve in Figure 6(d) (labeled  $\tau = 0.1$ ).

#### 4. Choice of Twist Parameter

For the parameter space study in this paper, we consider different combinations of the amplitude and sign of the twist parameter  $\tau$  introduced in Section 2.4. Our focus is to determine the global effect of different choices, rather than to optimize this choice against observational data. The latter is a significant challenge that is beyond the scope of this paper. In summary, the choices of  $\tau$  considered in our test simulations are as follows:

1. Constant magnitude and all regions follow the majority hemispheric sign rule (negative in the northern hemisphere, positive in the southern hemisphere). These runs are denoted  $\tau = 0.0, 0.05, 0.1, 0.2$ .
2. Constant magnitude, but each region has its observed sign. These runs are denoted  $\tau = 0.05 \text{ s}, 0.1 \text{ s}, 0.2 \text{ s}$ .
3. Both magnitude and sign for each region are derived from observations. These runs are denoted  $\tau = 2\alpha, 2.5\alpha, 3\alpha, 3.5\alpha, 4\alpha, 10\alpha$ .

The following subsections describe these cases in more detail.

##### 4.1. Constant Magnitude and Hemispheric Sign Rule

In the first set of simulations, we fix  $|\tau|$  to the same magnitude for all emerging regions. As an illustration of the effect of this parameter, Figure 7 shows the magnetic field structure after the emergence of an individual region in the magnetofrictional code, for four different values  $\tau = 0, -0.1, -0.4, 0.1$ . Each magnetic field line  $L$  is colored by its helicity contribution  $\mathcal{A}|B_r|$ , where

$$\mathcal{A} = \int_L \frac{\tilde{\mathbf{A}} \cdot \mathbf{B}}{|\mathbf{B}|} dl \quad (11)$$

is the field line helicity of the field line (Yeates & Hornig 2016), and  $|B_r|$  is averaged between the two endpoints of  $L$ . We use the vector potential  $\tilde{\mathbf{A}}$  (as in Section 3.3), in order that

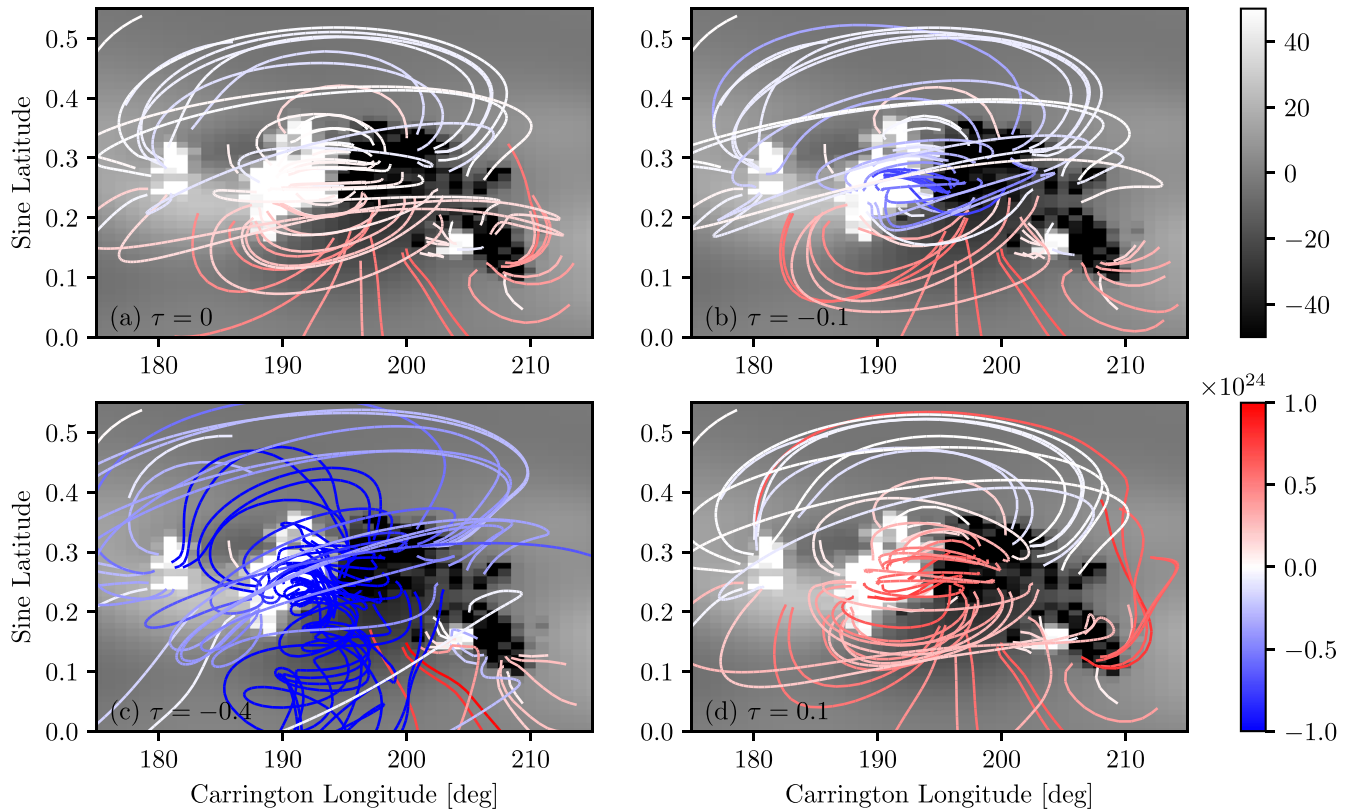


**Figure 7.** Effect of  $\tau$  parameter with  $T_{\text{em}} = 12$  hr. Field lines are colored red/blue to show  $\mathcal{A}|B_r|$ , clipped at  $\pm 10^{24}$  G<sup>2</sup> cm<sup>2</sup>, while black/white shading shows  $B_r$ , clipped at  $\pm 50$  G.

integrating  $\mathcal{A}|B_r|$  over both boundaries  $r = R_{\odot}$  and  $r = 2.5R_{\odot}$  would give (twice) the relative helicity (Yeates 2020b). The quantity  $\mathcal{A}|B_r|$  is a robust measure of the distribution of magnetic helicity within the corona, as both  $\mathcal{A}$  and  $|B_r|$  would be invariant during an ideal evolution in which the field line endpoints remained fixed. From Figure 7, we see that the amount and sign of helicity generated within the core of the active region are clearly controlled by the  $\tau$  parameter. Moreover, Figure 7(c) suggests that  $\tau = -0.4$  generates unphysically high twisting in the corona. We therefore consider four full test simulations with  $|\tau| = 0.0, 0.05, 0.1, 0.2$ .

Depending on the sign of the associated  $\tau$ , an emerging region will have either positive or negative helicity. Observational works (e.g., Pevtsov et al. 1995; Wang 2013; Park et al. 2020) have found that helicity of active regions, on average, follows the hemispheric rule, such that active regions in the northern and southern hemispheres are more likely to have negative and positive helicity, respectively. This is known as the hemispheric sign rule and is observed in other coronal features, too (Pevtsov et al. 2014). Thus, for this simplest set of simulations, we impose that all emerging regions strictly follow the hemispheric rule. Note that this does not preclude the formation of structures of the opposite sign of helicity as active regions spread out and interact. For example, in simulations with simplified bipolar active regions, Yeates & Mackay (2009) looked at the chirality of filament channels as active regions decay and interact. This chirality is a proxy for the sign of magnetic helicity and is observed to follow an even stronger hemispheric rule than active region helicity (Martin 1998; Mackay et al. 2010). It was found that reversing the sign of helicity in the emerging regions caused only 32% of the

simulated filament channels to reverse their chirality, highlighting how active region emergence is only one source of magnetic helicity in the corona.

#### 4.2. Constant Magnitude but Observed Sign

As mentioned above, observations show clearly that there are deviations from the hemispheric helicity sign rule in active regions (Wang 2013; Park et al. 2020). To explore the effect of such variations, we try a second set of simulations where  $|\tau|$  is still the same for all regions, but the sign of  $\tau$  is chosen for each individual region according to vector magnetogram observations. These vector data are not used in determining  $\mathbf{E}_{\perp}^0$  in Equation (2), but they can, in principle, give us physical information to constrain  $\Psi$ . In particular, the HMI/SHARP metadata provide the parameter  $\alpha_{\text{ob}} = \sum J_z B_z / (\sum B_z^2)$  (in  $\text{Mm}^{-1}$ ) for each region (Table 3 of Bobra et al. 2014). This does not correspond directly to the magnetic helicity of the region (which cannot be computed without further data) but is a proxy for the current helicity (integral of  $\mathbf{J} \cdot \mathbf{B}$ ), which represents the net local twisting of the magnetic field. The current helicity often, though not always, has the same sign as the magnetic helicity itself (Russell et al. 2019). The distributions of  $\alpha_{\text{ob}}$  in each hemisphere are depicted in Figure 8 for our test simulation period. We can see that among the 102 active regions during the simulation period, the majority follow the hemispheric sign rule (negative/positive in the North/South). However, we notice a significant number that deviate from the sign rule. Thus, in our second set of magnetofrictional simulations, we consider constant values of  $|\tau|$ , but with the sign chosen according to the observed sign of  $\alpha_{\text{ob}}$  for that region.

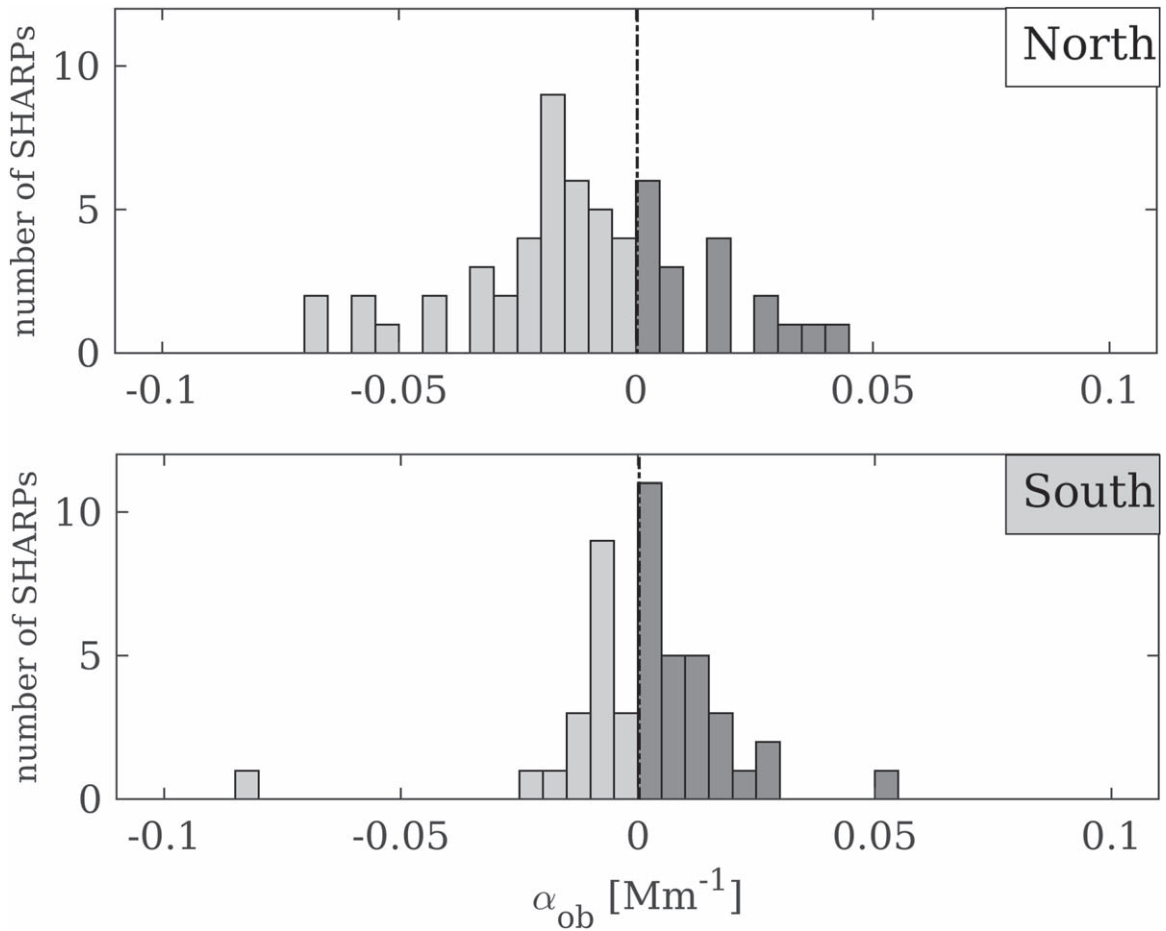


**Figure 8.** Distribution of  $\alpha_{\text{ob}}$  for the 102 observed HMI/SHARP regions, in  $0.005 \text{ Mm}^{-1}$  bins.

### 4.3. Observed Magnitude and Sign

In a more realistic simulation, emerging regions would not all have the same amplitude of twist. From the distribution of observed  $\alpha_{\text{ob}}$  (Figure 8), it is clear that active regions have diverse values of  $\alpha_{\text{ob}}$ , suggesting that diverse values of  $\tau$  are likely appropriate. This is also supported by computations of photospheric helicity flux in the literature (Georgoulis et al. 2009). As a first attempt to take this variation into account, we perform a third set of simulations where the  $\tau$  for each region is proportional to its observed value of  $\alpha_{\text{ob}}$  from the HMI/SHARPs metadata. We set  $\tau = c\alpha_{\text{ob}}$ , where the proportionality constant  $c$  has units of length.

To determine the best choice of  $c$ , we compare  $\alpha_{\text{ob}}$  for each of the 102 regions with the equivalent quantity  $\alpha_{\text{sm}}$  computed in the simulated region after emergence. Specifically, we define  $\alpha_{\text{sm}} = \sum J_r B_r / (\sum B_r^2)$  (in  $\text{Mm}^{-1}$ ) where  $J_r$  and  $B_r$  are calculated at  $r = 1.0154 R_{\odot}$ . To minimize the effect on  $\alpha_{\text{sm}}$  of any nonpotentiality in the surrounding (pre-existing) magnetic field, this computation is done not during the full simulation but independently for each region, emerging it into a potential field initialized on the day before emergence. The average quantity  $\alpha_{\text{sm}}$  is then computed at the end time of the emergence.

To compare  $\alpha_{\text{ob}}$  and  $\alpha_{\text{sm}}$  for each region, we check two factors: first, whether they have the same sign, and second, whether the ratio  $r_{\text{ob}}^{\text{sm}} = \alpha_{\text{sm}}/\alpha_{\text{ob}}$  is close to unity. Table 1 shows the results of evaluating the ratio when we use three alternative values of  $c$ : 2, 3, and 4 Mm. The first row shows the

**Table 1**  
Ratio between  $\alpha_{\text{sm}}$  and  $\alpha_{\text{ob}}$

$r_{\text{ob}}^{\text{sm}} = \alpha_{\text{sm}}/\alpha_{\text{ob}}$	$c = 2.0$	$c = 3.0$	$c = 4.0$
$r_{\text{ob}}^{\text{sm}} < 0.0$	19	15	15
$0.0 \leq r_{\text{ob}}^{\text{sm}} < 0.5$	18	15	12
$0.5 \leq r_{\text{ob}}^{\text{sm}} < 1.5$	31	33	31
$1.5 \leq r_{\text{ob}}^{\text{sm}} < 2.5$	12	12	12
$2.5 \leq r_{\text{ob}}^{\text{sm}} < 3.5$	7	11	12
$3.5 \leq r_{\text{ob}}^{\text{sm}} < 4.5$	3	3	5
$4.5 \leq r_{\text{ob}}^{\text{sm}} < 6.0$	1	3	3
$6.0 \leq r_{\text{ob}}^{\text{sm}}$	11	10	12

number of regions where  $\alpha_{\text{sm}}$  and  $\alpha_{\text{ob}}$  have opposite signs. Note that this number decreases from 19 to 15 with increasing  $c$ . The remaining rows depict the statistics where  $\alpha_{\text{sm}}$  and  $\alpha_{\text{ob}}$  have the same sign—true for more than 80% of regions. Those with ratios  $0.5 \leq r_{\text{ob}}^{\text{sm}} < 1.5$  best match observation, and we call them “good-fit” regions. Note that the maximum number of good-fit regions are obtained for  $c = 3.0 \text{ Mm}$ . Also, the number of regions with a very large ratio ( $r_{\text{ob}}^{\text{sm}} \geq 6.0$ ) is minimized when  $c = 3.0 \text{ Mm}$ . This suggests  $c = 3.0 \text{ Mm}$  is the optimum choice for the proportionality constant.

Even for the optimum choice of  $c$ , there are a considerable number of SHARP regions with a mismatch between  $\alpha_{\text{sm}}$  and  $\alpha_{\text{ob}}$ . We have investigated all of the regions where  $r_{\text{ob}}^{\text{sm}}$  deviated significantly from unity (either wrong sign or  $r_{\text{ob}}^{\text{sm}} \geq 1.5$ ), and

find that they fall into several classes. For example, 16 were tiny active regions where the value and sign of the simulated and observed  $\alpha$  will be heavily biased by a few grid points. Seven regions emerged very near to pre-existing active regions. A total of 11 regions had complex, mixed-polarity  $B_r$  distributions rather than simple bipoles, and six had two separate active regions within the same SHARP. The remaining 29 active regions were influenced by the current in the surrounding field. In particular, 15 among those 29 regions had the correct sign within the core of the region, but the overall measured  $\alpha_{sm}$  had either negative  $r_{ob}^{sm}$  or  $r_{ob}^{sm} < 0.5$ . For these regions, increasing the value of  $c$  reduced the discrepancy. The effect of “wrongly” imposed twist in the complex regions and SHARPs with two spots (total 17 regions) on the global scenario will be discussed later (in Section 5.2).

## 5. Results

The primary objective of these tests is to determine the effect of the free parameters in our magnetofrictional model, namely the emergence duration  $T_{em}$  and the twist  $\tau$ . Thus we perform multiple magnetofrictional simulations with the same model parameters and the same catalog of emerging regions, but with variations in  $T_{em}$  and  $\tau$ .

### 5.1. Effect of Emergence Duration

As prescribed in Section 2.2, each active region emerges over a time interval of duration  $T_{em}$ , during which a steady electric field  $E_{\perp}(s, \phi)$  is imposed. Note that, in any given simulation, our code uses the same value of  $T_{em}$  for all 102 active regions. While keeping the twist parameter fixed at  $\tau = \pm 0.1$  (negative for all regions in the northern hemisphere, positive for all regions in the southern hemisphere), we considered three different values of  $T_{em}$ : 6, 12, 24 hr. The effect is illustrated for an individual emerging region in Figure 9. We see that there is no qualitative difference in the magnetic field structure, the field line helicities (the colors of the field lines in the plot), or the current density distribution. However, we do see an increase in the peak current density when the emergence is carried out more rapidly, due to the reduced time for relaxation available. Another reason for the difference in current is the fact that supergranular diffusion continues to smooth out the photospheric field during the emergence process, at a rate independent of  $T_{em}$ .

The effect of choosing different  $T_{em}$  on the global diagnostics is shown in Figure 10, where we focus on a subinterval (September 2011) for clarity. In Figures 10(a) and (b), we find that decreasing the emergence duration, in general, corresponds to a little more magnetic energy and current density in the corona at the epochs of emergence (marked by the asterisks). However, these short-lived increments decay quickly, and the overall variation in energy and current density show significant similarities even with different  $T_{em}$ . Evolution of the other quantities, like open magnetic flux, helicity flux, and  $B_{\perp}$  in the northern and southern hemispheres (Figures 10(c)–(f)) do exhibit relatively higher differences. In particular, predictions of specific eruption timings from the model must be viewed as uncertain and likely require a more detailed assimilation of input data. Still, we notice no systematic overall effect of  $T_{em}$  on the global evolution when we consider the total time-integrated amplitude of open flux, helicity flux, the total  $B_{\perp}$  (in each hemisphere), and the total

number of peaks at the end of each simulation. The differences remain  $< 2.5\%$  for all of the time-integrated quantities when comparing the three simulations. Thus in the remainder of the paper, we fix the standard value  $T_{em} = 24$  hr, which is consistent with typical observations of sunspot emergence (van Driel-Gesztelyi & Green 2015).

### 5.2. Effect of Twist Parameter

We have performed 13 global magnetofrictional simulations with the same 102 emerging regions but different  $\tau$ , as described in Section 4. For each of these simulations,  $T_{em}$  was set at 24 hr. These comprise three sets of simulations with constant  $|\tau|$ : 0.0, 0.05, 0.1, 0.2 (sign according to the hemispheric rule), constant  $|\tau|$ : 0.05 s, 0.1 s, 0.2 s (sign according to observed sign of  $\alpha_{ob}$ ), and  $\tau = c \alpha_{ob}$ :  $2\alpha$ ,  $2.5\alpha$ ,  $3\alpha$ ,  $3.5\alpha$ ,  $4\alpha$ ,  $10\alpha$ . (The coefficients denote the proportionality constant  $c$  in Mm.) As stated previously, we primarily focus on the evolution of the global coronal magnetic field. Thus we compute the total time-integrated amplitude of open flux, total energy, average current density, helicity flux, average  $B_{\perp}$  (in each hemisphere), and the number of peaks in  $B_{\perp}$  (in each hemisphere). A detailed comparison of those quantities for individual simulations is depicted in Figure 11 where the horizontal axis represents different choices of  $\tau$ .

We can see that all of the measures have minimum amplitude when  $\tau = 0.0$ , which corresponds to  $E_{\perp} = E_{\perp}^0$ . Comparing the pair of simulations [0.05 & 0.05s], [0.1 & 0.1s], and [0.2 & 0.2s], we find that the simulations with signs of  $\tau$  according to observed  $\alpha_{ob}$  result in lower amplitudes of the total open flux, magnetic energy, current density, number of peaks, etc. (for example, see the pairs of data points highlighted by gray boxes Figure 11). The interpretation is that emerging regions with both signs of helicity tend to reduce the net coronal helicity in each hemisphere, allowing the coronal field to relax to a state with less free energy and current, leading to fewer and/or weaker eruptions.

The simulations where  $\tau = c \alpha_{ob}$  have increasing current, magnetic energy, and helicity flux with increasing  $c$ , and generally increasing numbers of eruptions. This increasing trend is visible in the data points encircled in Figure 11. Comparing the cases with constant  $|\tau|$  and  $\tau = c \alpha_{obs}$ , we can say that the case with  $c = 3.0$  Mm is globally similar to  $|\tau| = 0.05$  (with observed sign). On the other hand, the simulation with  $c = 10.0$  Mm is comparable with the  $|\tau| = 0.1$  simulation, although in this case the match between  $\alpha_{sm}$  and  $\alpha_{ob}$  is poorer (Section 4.3).

Not shown in Figure 11, we have performed additional global simulations with a higher constant twist amplitude,  $|\tau| = 0.4$  (with both uniform and observed signs). With such strong twists, most of the active regions erupt immediately after emergence, and we feel that the observed twisting of magnetic field lines is unrealistically high compared to typical observations of coronal loops. This excessive twist is illustrated in Figure 7(c). As such, we feel that the simulations with  $|\tau| = 0.1$  or  $\tau = 10\alpha_{ob}$  provide a rough upper limit to the reasonable amount of helicity that should be injected into the emerging regions.

As we noted in Section 4.3, the ratios  $r_{ob}^{sm}$  for a number of regions with complex  $B_r$  distributions differed substantially from the ideal value of unity. Of these regions, 17 were either complex multipolar regions or SHARPs containing two separate active regions. Hence to evaluate the effect of the

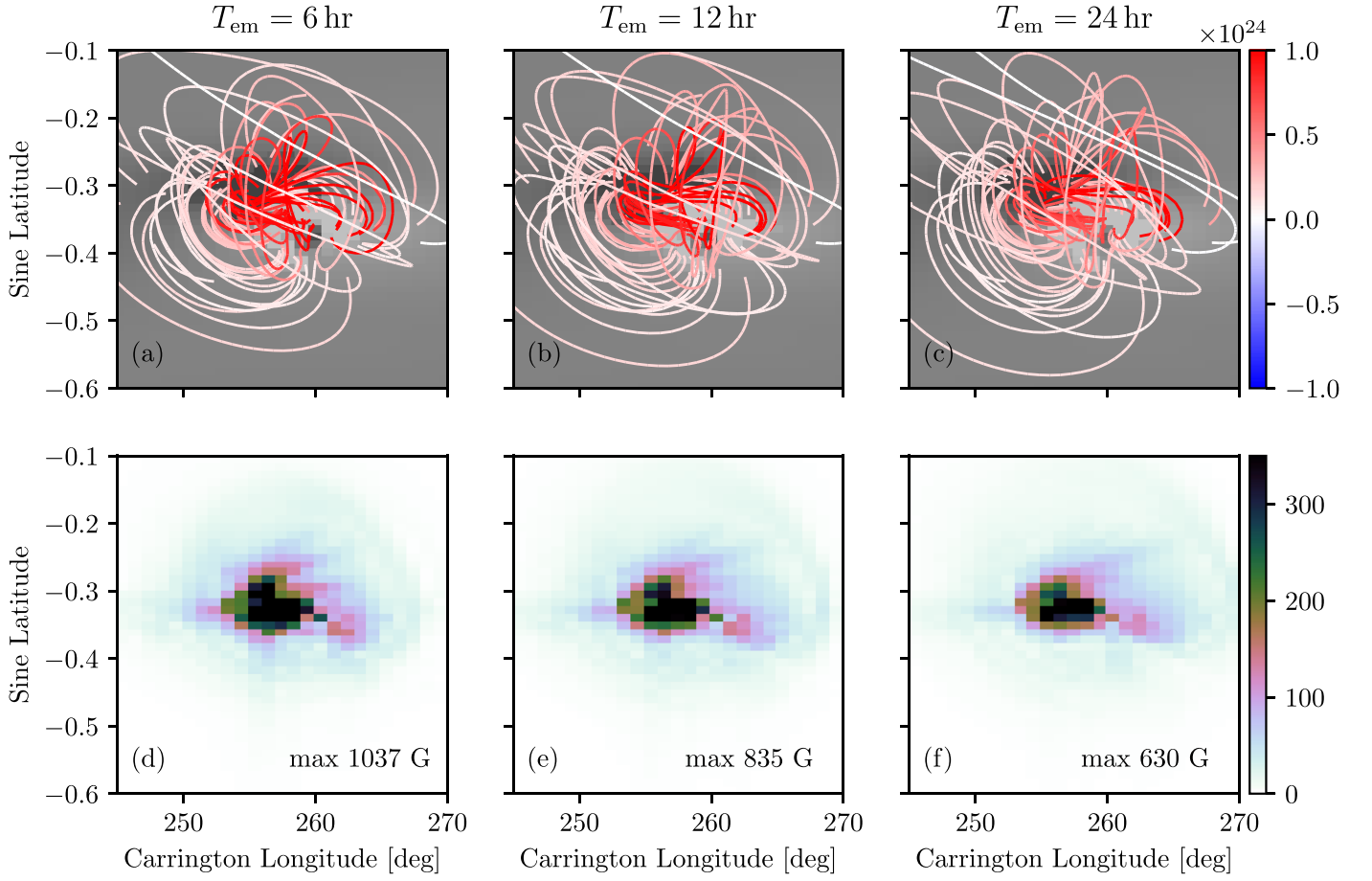


**Figure 9.** Effect of the  $T_{\text{em}}$  parameter on an emerged region (SHARP 824), with  $\tau = 0.1$ . Columns from left to right show the active region at the end of the emergence process, for  $T_{\text{em}} = 6, 12, 24$  hr, respectively. Panels (a)–(c) show  $B_r$  on the solar surface (grayscale) and magnetic field lines colored by  $A|B_r|$  (in  $\text{G}^2 \text{cm}^2$ ). Panels (d)–(f) show the line-of-sight integrated current density,  $F = \int_{R_{\odot}}^{1.5R_{\odot}} |\nabla \times \mathbf{B}|^2 dr$ , where the color bar is capped at  $F = 350$  G in order to show weaker structures. Actual maximum values of  $F$  are given in the figures.

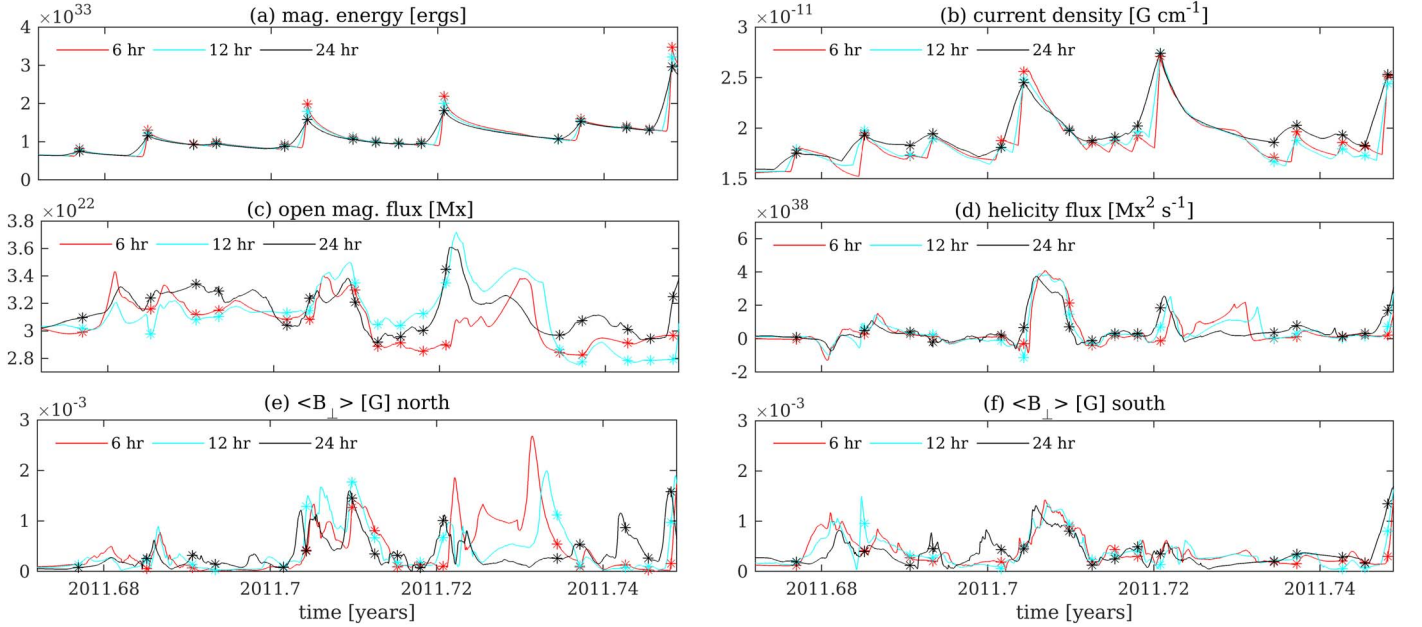


**Figure 10.** Effect of the  $T_{\text{em}}$  parameter on the temporal evolution of the global quantities during 2011 September. In every plot, red, cyan, and black curves correspond to  $T_{\text{em}} = 6, 12, 24$  hr, respectively, with fixed  $\tau = 0.1$  for all SHARPs. The asterisks denote the emergence epoch of the SHARPs during that period. Different columns represent the temporal evolution of (a) total magnetic energy, (b) mean current density, (c) unsigned open magnetic flux, (d) helicity flux through the outer boundary, (e) and (f) horizontal components of the magnetic field at the outer boundary in the northern and southern hemispheres, respectively.

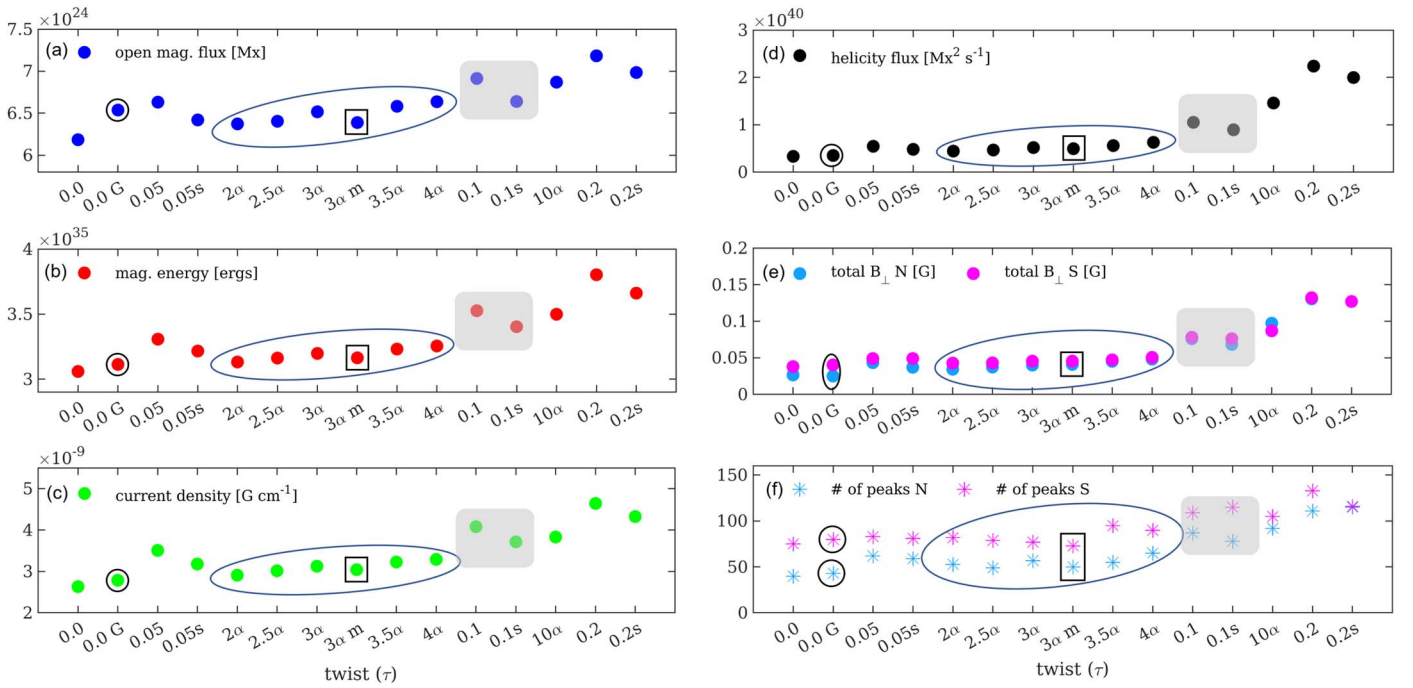


**Figure 11.** Global diagnostics for the simulations with different  $\tau$ . For the number of peaks, we choose the threshold  $B_{\perp} = 1 \times 10^{-4}$  G. The run labeled 0.0 G uses the global inductive  $E_{\perp}$  (Section 5.3), and  $3\alpha$  m has a twist set to zero for 17 selected regions (see text).

“wrong” twist of these regions on the global scenario, we ran a further global simulation with the twist of these regions set to zero and the remaining 85 regions left as  $\tau = 3.0 \alpha_{\text{ob}}$ . This modification causes slight decreases in the total open flux (2%), magnetic energy (1%), and current density (2.7%). Interestingly, quantities closely associated with eruptions through the upper boundary showed somewhat more significant effects: total helicity flux was reduced by 4.2%, and the number of peaks in  $B_{\perp}$  decreased by 5.2% and 12.3% in the northern and southern hemispheres, respectively (see the data points within individual rectangles and corresponding to  $\tau: 3\alpha$  m in Figure 11). This gives an indication of the importance of choosing  $\tau$  carefully.

### 5.3. Comparison to Global Inductive Solution

Lastly, we performed two more simulations with constant  $|\tau| = 0.0$  and  $0.1$  (with signs according to the hemispheric rule) but used the global inductive solution to compute  $E_{\perp}$  for each of the active regions (see Figures 3(c) and (g)). Even for the run with  $\tau = 0.0$ , the global inductive simulation generated higher amounts of total open flux (5.3%), magnetic energy (1.6%), current density (5.4%), and helicity flux (4.9%), as well as more peaks in  $B_{\perp}$  (North: 6.9% and South: 5.5%) as compared to the local solution (see the data points corresponding to  $\tau = 0.0$  G, which are encircled separately in Figure 11). Running another such simulation with  $\tau = 0.1$  (hemispheric signs) only for 2011 June revealed that the differences increased further when the chosen twist amplitude was higher.

## 6. Conclusion

In this paper we have presented a technique for emerging active regions in solar coronal simulations using electric fields on the lower boundary. Our “local inductive” electric field solution avoids the disadvantages of existing electric field inversion methods when applied in the global solar corona. On

the one hand, it avoids spurious nonlocalization that would occur in an inductive electric field computed over the full sphere, but on the other hand it is more robust and computationally efficient than a sparse ( $L_1$ -minimizing) electric field (Yeates 2017). As such, spurious coronal electric currents are minimized when this new electric field is used to drive continuously evolving coronal simulations. Compared to previous such simulations where active regions were approximated with idealized magnetic bipoles, the new technique allows for arbitrary patterns of  $B_r$  on the solar surface, without the need for manual fitting.

Although our basic “local inductive” electric field has the advantage of requiring only line-of-sight magnetogram data, we have also explored the (indirect) use of vector magnetogram observations for choosing the helicity of individual active regions. This we control through a parametrized noninductive component of the electric field. Previously, global simulations have either neglected active region helicity or chosen it at random for each magnetic bipole. Our test simulations include runs with and without the use of vector data. In the latter case, we simply use the same twist parameter for all regions (accounting only for the hemispheric helicity sign). We have determined the parameter values needed for the two techniques to give comparable global properties.

Our focus has been on describing the new emergence method and determining a reasonable choice of parameters, especially the helicity/twist parameter. In particular, it is beyond the scope of this paper to compare the resulting nonpotential coronal magnetic field with the real Sun. This is a challenging task that will need to be addressed in the future; it will almost certainly rely on indirect means such as the chirality of solar filaments (Yeates & Mackay 2009), the morphology of extreme-ultraviolet structures (Meyer et al. 2020), or possibly the open magnetic flux and heliospheric sector structure inferred from solar wind measurements (Gonzi et al. 2021).

This challenge applies, of course, to any other model of the coronal magnetic field.

Although the new emergence technique has been tested using magnetofrictional simulations where the coronal magnetic field responds in a quasi-static fashion to photospheric driving, the application of the technique is not limited to this method. In particular, it could be used to drive dynamical MHD simulations with appropriate boundary conditions for the additional variables. Thanks to the limited magnetogram input required, it will be useful also for simulations where fewer data are available—for example, hypothetical models of future activity, past activity (e.g., the Maunder minimum, Riley et al. 2015), or of other stars (e.g., Gibb et al. 2016).

Because the emergence process remains highly parameterized, based on a single magnetogram per region, it is not suited to studies of coronal dynamics in young active regions. Such studies require higher resolution data in both space and time and are typically restricted to individual active regions for computational reasons, although models are being developed that couple such models into global-scale simulations (e.g., Hoeksema et al. 2020). Thus the technique is better suited for probing the nature of the global corona on longer timescales, rather than focusing on specific events. We have seen that the emergence parameters (duration and twisting) can and do affect the evolution of the coronal magnetic field. While the emergence duration changes only local details and not the overall level of nonpotentiality, we find that the choice of twisting parameter for each active region has a significant effect on all of the global measures of the coronal magnetic field that we considered.

Although we have explored how to account for observed vector magnetogram information in choosing the twisting parameter, it must be acknowledged that the observational constraint here, coming from the  $\alpha_{\text{ob}}$  parameter in the HMI/SHARP metadata, could be strengthened. For many active regions, the provided uncertainty in this parameter from HMI is similar in magnitude to, or larger than, the parameter itself. A further issue is that  $\alpha_{\text{ob}}$  does not correlate directly to the magnetic helicity, which is the physical property that we would ultimately like to constrain. Nevertheless, we do hope that accounting for  $\alpha_{\text{ob}}$  does give improved fidelity to the model, at least in active regions where the pattern of electric current is reasonably coherent. In future applications it may be worthwhile to develop automated criteria for whether or not to make the twist parameter proportional to  $\alpha_{\text{ob}}$  in any given region. In principle it would be possible to give a better estimate of the observed helicity using higher-cadence electric field inversion along with the use of vector magnetogram and Doppler velocity observations (Fisher et al. 2020), although this may not be practical in long-duration simulations. There is also the systematic issue that, with present observations, the helicity content can be derived in this way only for regions whose full evolution can be followed on the visible solar disk. In global simulations, the emergence technique needs to cope with all active regions, so we feel that there will continue to be a role for parametrized approaches such as we have described.

This work was supported by UK STFC grants ST/S000321/1 and ST/V00235X/1. The SDO data are courtesy of NASA and the SDO/HMI science team. This work has made use of the Hamilton HPC Service of Durham University. ARY would like to thank D. H. Mackay for useful discussions regarding the

helicity injection method. We thank the anonymous referee for their useful suggestions.

*Facilities:* SDO (HMI).

## ORCID iDs

Anthony R. Yeates  <https://orcid.org/0000-0002-2728-4053>  
Prantika Bhowmik  <https://orcid.org/0000-0002-4409-7284>

## References

- Bhowmik, P., & Yeates, A. R. 2021, *SoPh*, 296, 109  
 Bobra, M. G., Sun, X., Hoeksema, J. T., et al. 2014, *SoPh*, 289, 3549  
 Cheung, M. C. M., & DeRosa, M. L. 2012, *ApJ*, 757, 147  
 Fan, Y., & Gibson, S. E. 2004, *ApJ*, 609, 1123  
 Fisher, G. H., Kazachenko, M. D., Welsch, B. T., et al. 2020, *ApJS*, 248, 2  
 Fisher, G. H., Welsch, B. T., & Abbett, W. P. 2012, *SoPh*, 277, 153  
 Fisher, G. H., Welsch, B. T., Abbett, W. P., & Bercik, D. J. 2010, *ApJ*, 715, 242  
 Georgoulis, M. K., Rust, D. M., Pevtsov, A. A., Bernasconi, P. N., & Kuzanyan, K. M. 2009, *ApJL*, 705, L48  
 Gibb, G. P. S., Mackay, D. H., Jardine, M. M., & Yeates, A. R. 2016, *MNRAS*, 456, 3624  
 Gonzi, S., Weinzierl, M., Bocquet, F. X., et al. 2021, *SpWea*, 19, e02499  
 Hayashi, K. 2013, *JGRA*, 118, 6889  
 Hayashi, K., Abbett, W. P., Cheung, M. C. M., & Fisher, G. H. 2021, *ApJS*, 254, 1  
 Hayashi, K., Feng, X., Xiong, M., & Jiang, C. 2018, *ApJ*, 855, 11  
 Hoeksema, J. T., Abbett, W. P., Bercik, D. J., et al. 2020, *ApJS*, 250, 28  
 Iijima, H., Hotta, H., & Imada, S. 2019, *ApJ*, 883, 24  
 Jiang, J., Song, Q., Wang, J.-X., & Baranyi, T. 2019, *ApJ*, 871, 16  
 Kazachenko, M. D., Fisher, G. H., & Welsch, B. T. 2014, *ApJ*, 795, 17  
 Lowder, C., & Yeates, A. 2017, *ApJ*, 846, 106  
 Lumme, E., Pomoell, J., & Kilpua, E. K. J. 2017, *SoPh*, 292, 191  
 Lumme, E., Pomoell, J., Price, D. J., et al. 2022, *A&A*, 658, A200  
 Mackay, D. H., DeVore, C. R., Antiochos, S. K., & Yeates, A. R. 2018, *ApJ*, 869, 62  
 Mackay, D. H., Green, L. M., & van Ballegooijen, A. 2011, *ApJ*, 729, 97  
 Mackay, D. H., Karpen, J. T., Ballester, J. L., Schmieder, B., & Aulanier, G. 2010, *SSRv*, 151, 333  
 Mackay, D. H., & van Ballegooijen, A. A. 2001, *ApJ*, 560, 445  
 Mackay, D. H., & van Ballegooijen, A. A. 2005, *ApJL*, 621, L77  
 Mackay, D. H., & Yeates, A. R. 2021, *SoPh*, 296, 178  
 Martin, S. F. 1998, *SoPh*, 182, 107  
 Metcalf, T. R., De Rosa, M. L., Schrijver, C. J., et al. 2008, *SoPh*, 247, 269  
 Metcalf, T. R., Leka, K. D., Barnes, G., et al. 2006, *SoPh*, 237, 267  
 Meyer, K. A., Mackay, D. H., Talpeanu, D.-C., Upton, L. A., & West, M. J. 2020, *SoPh*, 295, 101  
 Mikić, Z., Downs, C., Linker, J. A., et al. 2018, *NatAs*, 2, 913  
 Park, S.-H., Leka, K. D., & Kusano, K. 2020, *ApJ*, 904, 6  
 Pevtsov, A. A., Berger, M. A., Nindos, A., Norton, A. A., & van Driel-Gesztelyi, L. 2014, *SSRv*, 186, 285  
 Pevtsov, A. A., Canfield, R. C., & Metcalf, T. R. 1995, *ApJL*, 440, L109  
 Pomoell, J., Lumme, E., & Kilpua, E. 2019, *SoPh*, 294, 41  
 Rice, O. E. K., & Yeates, A. R. 2021, *ApJ*, 923, 57  
 Riley, P., Lionello, R., Linker, J. A., et al. 2015, *ApJ*, 802, 105  
 Russell, A. J. B., Demoulin, P., Hornig, G., Pontin, D. I., & Candelaresi, S. 2019, *ApJ*, 884, 55  
 Sun, X. 2018, arXiv:1801.04265  
 van Ballegooijen, A. A., & Cranmer, S. R. 2008, *ApJ*, 682, 644  
 van Ballegooijen, A. A., Priest, E. R., & Mackay, D. H. 2000, *ApJ*, 539, 983  
 van Driel-Gesztelyi, L., & Green, L. M. 2015, *LRSP*, 12, 1  
 Virtanen, I. I., Pevtsov, A. A., & Mursula, K. 2019, *A&A*, 624, A73  
 Wang, Y. M. 2013, *ApJL*, 775, L46  
 Weinzierl, M., Yeates, A. R., Mackay, D. H., Henney, C. J., & Arge, C. N. 2016, *ApJ*, 823, 55  
 Wiegmann, T., & Sakurai, T. 2021, *LRSP*, 18, 1  
 Yang, L. P., Feng, X. S., Xiang, C. Q., et al. 2012, *JGRA*, 117, A08110  
 Yardley, S. L., Mackay, D. H., & Green, L. M. 2018, *ApJ*, 852, 82  
 Yardley, S. L., Mackay, D. H., & Green, L. M. 2021, *SoPh*, 296, 10  
 Yeates, A. 2018, antyeates1983/pfss: First release of pfss code v.1.0, Zenodo, doi:10.5281/zenodo.1472183  
 Yeates, A. 2022, antyeates1983/sharps-bmrs: Release for Zenodo v1.0.1, Zenodo, doi:10.5281/zenodo.6556401  
 Yeates, A. R. 2014, *SoPh*, 289, 631

Yeates, A. R. 2017, [ApJ](#), 836, 131

Yeates, A. R. 2020a, [SoPh](#), 295, 119

Yeates, A. R. 2020b, [ApJL](#), 898, L49

Yeates, A. R., Amari, T., Contopoulos, I., et al. 2018, [SSRv](#), 214, 99

Yeates, A. R., & Hornig, G. 2016, [A&A](#), 594, A98

Yeates, A. R., & Mackay, D. H. 2009, [SoPh](#), 254, 77

Yeates, A. R., Mackay, D. H., & van Ballegoijen, A. A. 2008, [ApJL](#), 680, L165